

Electrodeposited Magnetic Nanoporous Membrane (MNM) with a Multi-Edge Superparamagnetic Heterogeneous Wedge Junction for High-Yield and High-Throughput Immunocapture of Specific Extracellular Vesicles and Lipoproteins

Chenguang Zhang

University of Notre Dame <https://orcid.org/0000-0001-5124-875X>

Xiaoye Huo

University of Notre Dame

Yini Zhu

University of Notre Dame

James Higginbotham

Xin Lu

Jeffrey Franklin

Kasey Vickers

Robert Coffey

Satyajyoti Senapati

University of Notre Dame

Ceming Wang

Hsueh-Chia Chang (✉ hchang@nd.edu)

University of Notre Dame <https://orcid.org/0000-0003-2147-9260>

Article

Keywords: Extracellular Vesicle, Superparamagnetic, Immunocapture

Posted Date: June 3rd, 2022

DOI: <https://doi.org/10.21203/rs.3.rs-1448269/v2>

License: © ⓘ This work is licensed under a Creative Commons Attribution 4.0 International License.

[Read Full License](#)

1 **Electrodeposited Magnetic Nanoporous Membrane (MNM) with a**
2 **Multi-Edge Superparamagnetic Heterogeneous Wedge Junction for**
3 **High-Yield and High-Throughput Immunocapture of Specific**
4 **Extracellular Vesicles and Lipoproteins**

5 Chenguang Zhang^{1,#}, Xiaoye Huo^{1,#}, Yini Zhu², James N. Higginbotham³, Xin Lu², Jeffrey L. Frank-
6 lin^{3,4}, Kasey C. Vickers³, Robert J. Coffey^{3,4}, Satyajyoti Senapati¹, Ceming Wang^{5,*}, Hsueh-Chia
7 Chang^{1,*}

8 ¹ Department of Chemical and Biomolecular Engineering, University of Notre Dame, Notre Dame, IN 46556,
9 USA.

10 ² Department of Biology, University of Notre Dame, Notre Dame, IN 46556, USA.

11 ³ Department of Medicine, Vanderbilt University Medical Center, Nashville, TN 37232, USA.

12 ⁴ Department of Cell and Developmental Biology, Vanderbilt University School of Medicine, Nashville, TN
13 37232, USA.

14 ⁵ Aopia Biosciences, 31351 Medallion Dr, Hayward, CA 94544, USA.

15 # These authors contributed equally: Chenguang Zhang, Xiaoye Huo.

16 corresponding author email: cwang9@nd.edu, hchang@nd.edu

17 **Abstract.** Superparamagnetic nanobeads offer several advantages over microbeads for immunocapture of specific
18 molecular nanocarriers (extracellular vesicles, lipoproteins, and viruses) in a bioassay: high-yield capture, reduction
19 in incubation time, and higher capture capacity. However, nanobeads are difficult to “pull-down” because their su-
20 perparamagnetic feature requires high nanoscale magnetic field gradients in addition to high magnetic fields. Here,
21 an electroplated track-etched membrane is shown to produce a unique superparamagnetic nano edge ring with mul-
22 tiple edges around each nanopore. With a uniform external magnetic field, the induced monopole and dipole of this
23 nano edge junction combine to produce a 10x higher nanobead trapping force. A dense nanobead suspension can be
24 filtered through the magnetic nanoporous membrane (MNM) at high throughput with a 99% bead capture rate. The
25 capture yield of specific nanocarriers in heterogeneous media (filtered plasma and conditioned cell media) by nano-
26 beads/MNM exceeds 80%. Quantification of RNA cargo in captured extracellular vesicles demonstrates a 60x in-
27 crease in the capture rate of a specific microRNA relative to magnetic bead columns. Reproducibility, low loss, and
28 concentration-independent capture rates are also demonstrated. This new MNM material hence significantly expands
29 the application of nanobead immunocapture to heterogeneous physiological samples, such as plasma and saliva.

30 **Keywords:** Extracellular Vesicle, Superparamagnetic, Immunocapture

31

32 **1 Introduction**

33 Extracellular vesicles (EVs) and lipoproteins are biological nanoparticles that can be found in various
34 biological fluids¹⁻³. Their recently discovered function of delivering molecular cargo between cells has
35 catalyzed considerable research activity in many fields^{4,5}. These biological nanocarriers may be critical
36 mediators of intercellular communication^{6,7}. Thus, specific EVs, lipoproteins, and their molecular cargos
37 are also potential disease biomarkers⁸⁻¹⁰. However, these biomarkers are often not unique to diseased
38 cells but are simply overexpressed. Consequently, precise quantification is required. Due to their size
39 and heterogeneity, high-yield isolation of specific EVs and lipoproteins remains challenging and may
40 introduce significant bias in the biomarker assay¹¹⁻¹⁵. EVs and lipoproteins also tend to degrade, aggre-
41 gate, or adsorb in many devices^{16,17}. Thus, immediate and short-contact isolation is preferred over flow
42 cytometry and chromatography separation, whose pre-treatment/separation processes are long and com-
43 plex. An effective, rapid, and accessible isolation method is hence a prerequisite for any clinical appli-
44 cation involving EVs and lipoproteins. Advances in high-yield capture technologies are beneficial across
45 many biomedical spaces, including for the detection of pathogenic viruses or bacteria.

46

47 The most specific EV and lipoprotein isolation method is immunocapture¹⁸⁻²⁰; however, traditional
48 immuno-capture technologies, like immuno-precipitation (IP) and immunoaffinity chromatography,
49 have low-yield issues due to probe saturation and analyte loss. If the nanocarriers are fluorescently la-
50 beled, those captured by magnetic microbeads can be sorted and quantified by flow cytometry. However,
51 the labeling and isolation process is time-consuming and may require more than one day to achieve the
52 optimal yield, resulting in significant nanocarrier loss. Their throughputs are also limited by the long
53 incubation time (8-48 hrs) because of the low mobility of microbeads for the transport-limited docking
54 reaction. A solution to the yield and incubation time issues is to use nanomagnetic beads. Their large
55 surface area per volume provides more binding sites. Their smaller size leads to higher diffusivity and a
56 shorter incubation time (approximately 30min). The beads can also diffuse through a heterogeneous
57 physiological sample to capture specific nanoparticle targets that have reduced mobility due to

58 complexification or aggregation. Their large surface area per volume provides more binding probes by a
59 factor equal to the ratio of the microbead/nanobead radii (~ 100) for the same bead weight concentration.
60 This significant increase in the probe number can lead to complete depletion of all the target nanocarriers,
61 particularly if the antibody probes have high affinity, thus providing orders of magnitude higher nanocarrier
62 binding yield.

63

64 However, due to their superparamagnetic nature, it is difficult to trap nanobeads and their captured
65 nanocarriers after bulk immuno-capture. The magnetic force on the superparamagnetic beads is proportional
66 to the gradient of field squared (twice the product of the field and field gradient), whereas the force
67 on a magnetic microbead is proportional to the local field. For the commonly used magnetic microbead
68 traps, the field gradient is confined to less than one radius of the microbead and hence, can only trap
69 nanobeads within a small area around the microbead. Therefore, a long column of densely packed beads
70 is required for high-yield capture. For example, commercial microbeads columns (μ Column, Milyteni
71 Biotech) for nanobead capture only trap 20-30% of the nanobeads²¹. Repeated ($>4x$) trapping is necessary
72 to produce $> 90\%$ yield. A magnetic film can produce a higher field penetration length than a magnetic
73 bead due to its non-focusing (non-radial) geometry. Recently, Issadore and colleagues developed a
74 magnetic layer-coated nanoporous membrane with improved capture yield, but multiple layers of membranes
75 are still required for efficient bead capture²². Although the field is long-range, the field gradient
76 is not for a planar magnetic film, except at corners. In our earlier work on electric fields at microchannels²³
77 and nanopores²⁴, we showed that a singular electric field with a high gradient occurs in the high
78 permittivity (water) side of a wedge corner of a channel or a pore if the wedge angle α of the higher
79 permittivity phase exceeds π . This wedge singular field decays radially from the wedge tip with a power-law
80 scaling of $-(\pi/\alpha) - 1$ and hence also has a high field gradient. The radial decay exponent is bound
81 between -2 of a sphere and -3/2 of an infinitely long cylinder. This singular wedge mode is antisymmetric
82 around the wedge and introduces a dipole in the high permittivity phase. There is a more well-known
83 “lightning rod” wedge singularity in near-field plasmonics²⁵⁻²⁷ that is symmetric around the wedge, with
84 the singular field occurring on the low permittivity side. It occurs when the high-permittivity side has a
85 wedge angle that is less than π . It introduces a monopole on the low-permittivity side of the wedge.
86 Herein, we extend this concept to magnetic fields to achieve high-yield capture of superparamagnetic

87 beads with high throughput. We designed a multi-edge superparamagnetic NiFe nano edge with a hetero-
 88 geneous junction, whose edges sustain both a magnetic monopole and dipole around each nanopore of
 89 a nanoporous polymer membrane. This approach will significantly increase the capture yield of one
 90 membrane to 99% at a throughput of 5mL/hr for a single magnetic nanoporous membrane (MNM).

91

92 Compared to the smooth pore edge formed during sputtering, edges on the electroplated membrane
 93 are sharper to approach the wedge geometry. Therefore, electroplating was used instead of sputtering for
 94 Ni₈₀Fe₂₀ layer deposition. Moreover, because of the high field at the Au film junction during electroplat-
 95 ing, the NiFe film wraps around the gold layer sputtered inside the pore to form the desired edge geom-
 96 etry for a dipole. The uncaptured EVs can go through the straight pores and be collected in the flow-
 97 through. We proved MNM's efficiency and specificity using high-density lipoproteins (HDL) as a model
 98 and observed that >80% of HDL is recovered using the method, nearly doubling the recovery rate for
 99 commercial kits. We also demonstrated that MNM has a high and consistent yield and hence, can provide
 100 the necessary statistics for quantifying biomarkers carried by EVs and lipoproteins in heterogeneous
 101 physiological fluids.

102

103 2 Results

104 2.1 Theory and Simulation of Heterogeneous Superparamagnetic Nano-Junction

105 Because the magnetic moment of a superparamagnetic nanobead is induced by the external field, the
 106 force on it is described by:

$$107 \quad \vec{F}_M = \frac{\chi_{eff} V \mu}{2\mu_0} \nabla |\vec{B}|^2 \quad (1)$$

108 Where χ_{eff} is the effective magnetic susceptibility of the beads, V is the bead volume, μ and μ_0 are the
 109 vacuum and material magnetic permittivity, and \vec{B} is the magnetic field. The magnetic force increases as
 110 the gradient of the field squared or twice the field multiplied by the field gradient. Thus, a high magnetic
 111 field gradient is the key to achieving high bead recovery. The geometric enhancement of electromagnetic
 112 field has been applied to a variety of engineering designs, from large-scale antenna^{28,29} to nanostruc-
 113 tures^{30,31}. Previously, we used the singular electric field at the edge of microchannels²³ and nanopores²⁴
 114 to trap colloids and translocate molecules by dielectrophoresis. As shown in Figure 1a and c, the edge of

115 the nanopore on the sputtered membrane is smooth. The NiFe layer only covered the top of the Au layer
116 due to the anisotropic nature of sputtering. A sharper edge appeared in the electroplated membrane be-
117 cause of the electric field focusing during plating (Figure 1b and d). The NiFe film also grew inside the
118 pore to form the wedge heterogeneous junction since, unlike sputtering, electroplating also occurs on the
119 side of the 80nm gold film. Under uniform external magnetization at 0.4 Tesla, a maximum field of 0.62
120 Tesla and a maximum gradient of flux density square at $2.3 \times 10^5 \text{ T}^2/\text{cm}$ develops in the water phase
121 (Figure 1h), compared to 0.48 Tesla and $2.2 \times 10^4 \text{ T}^2/\text{cm}$ for the sputtered NiFe film without the wedge
122 ring, which represents a 10-fold increase in the force field of Equation (1).

123

124 The high field enhancement originates from a water phase monopole at the upper edge of the NiFe
125 film, where the wedge angle on the high permeability superparamagnetic NiFe phase is approximately
126 $\pi/2$, and a dipole in the NiFe phase at the outer edge at the base of the wedge junction, where the wedge
127 angle on the NiFe side is approximately $3\pi/2$. There is an additional amplification of the dipole field
128 as it enters into the water phase with a magnetic permeability that is 40 times lower. In the sputtered
129 membrane, we only have a weak upper monopole due to the smooth edge (Figure 1g). This combination
130 of the dipole and monopole field at the sharp edges of the electroplated NiFe film is responsible for the
131 10x increase in the nanobead trapping force, and we expect to observe a similar increase in capture yield
132 for superparamagnetic nanobeads.

133

134 2.2 High-Efficiency Capture of Superparamagnetic beads by MNM

135 To test the capture efficiency of the MNM with the multi-edge superparamagnetic wedge around each
136 nanopore, we designed a housing apparatus for MNM immuno-capture applications, which is described
137 in the supporting information. Round membranes with 2cm diameter were tested during the experiments.
138 Briefly, 1mL of $10 \times$ diluted 30 nm nanobeads from Exosome Isolation Kit Pan (mouse, Miltenyi Biotec)
139 were passed through the electroplated 450nm (PET pore size) nanoporous membrane at 1mL/hr. Figure
140 2b shows the bead solution before and after magnetic capturing on the membrane; the brownish bead
141 color disappears entirely in the flow-through solution, indicating high bead capture efficiency. Nano-
142 beads convected by streamlines close to the surface are trapped by the monopole near the top edge of the

143 NiFe film, as shown in Figure 2a. The remaining beads are convected into the pore center and are trapped
144 by the high dipole magnetic force within the pore (Figure 2c).

145

146 The pore size shrinks from 450nm to about 350nm after electroplating, which is still larger than the
147 typical small EV (sEV) size of 30-200 nm, allowing non-target EVs without nanobeads to pass through.
148 A quantitative study of bead capturing efficiency was conducted by comparing the bead concentration
149 measured by nanoparticle tracking analysis (NTA) before and after capturing (see Figure 2e). At 1mL/hr,
150 >99% of the beads were captured. The bead capture efficiency did not diminish even at a flow rate of
151 5mL/hr. This throughput is high enough for most extracellular vesicle immuno-capture applications. Fur-
152 thermore, only 13% of the beads were lost when the flow rate was increased to 10mL/hr. For membranes
153 with 1 μ m pore size, the bead capture efficiency was still >80% at 1mL/hr. In stark contrast, only 22% of
154 beads were captured by the sputtered 450nm membrane (Figure 2e). For larger vesicles above 300nm,
155 electroplated MNM with 1 μ m pore size can be used at a lower flow rate or with a higher external mag-
156 netic field.

157

158 **2.3 Isolation of High-Density Lipoprotein (HDL)**

159 Based on the effectiveness of the MNM in capturing EVs, we sought to investigate the capacity of this
160 method to capture lipoproteins, namely HDLs. HDLs are highly-abundant in plasma and other biofluids
161 and provide a good model to trace based on standard cholesterol assays that can be used to quantify them.
162 Apolipoprotein A-I (apoA-I) is the main structure-function protein on the surface of HDL particles.
163 ApoA-I is primarily associated with HDL and accounts for approximately 70% of total HDL protein
164 content by mass. HDL samples were isolated from human plasma by density-gradient ultracentrifugation
165 (DGUC), and total protein levels were quantified by colorimetric assays³². For capture, 2 μ g anti-ApoA-
166 I (Abcam, ab52945, rabbit monoclonal to ApoA1) antibodies were mixed with 100 μ L of 100 μ g/mL HDL
167 sample, incubated for 30min, and treated with 100 μ L anti-rabbit IgG nanobeads (30nm, Milyteni Bio-
168 tech) for 1 hr. After the HDL was immuno-captured by the magnetic nanobeads, the solution was diluted
169 to 500 μ L with 1 \times PBS and passed through the 450nm electroplated MNM membrane, followed by flush-
170 ing with 1mL 1 \times PBS to bring all beads onto the membrane surface and to remove the residual HDL
171 solution in the chamber. The flow-through was collected for each sample. The concentration of

172 cholesterol was measured to calculate the total amount of cholesterol in both the original sample and
 173 flow-through (Figure 3b). The cholesterol capture rate can be calculated as:

$$174 \quad \text{Cholesterol Captured \%} = \frac{\text{Cholesterol}_{\text{original}} - \text{Cholesterol}_{\text{flow-through}}}{\text{Cholesterol}_{\text{original}}} \times 100\% \quad (2)$$

175 Remarkably, >80% of HDL was recovered using this approach. To confirm the specificity of the im-
 176 muno-capture and non-specific adsorption in our device, two negative controls were tested. If no anti-
 177 bodies were functionalized onto the nanobeads in the experiments, < 10% of HDL was lost in the device,
 178 which was due to non-specific adsorption and experimental error. When antibodies against apolipoprotein
 179 B (ApoB), the structural protein for low-density lipoproteins (LDL), were used instead of anti-ApoA-
 180 I, the loss increased to 14%. The additional 4% loss may come from non-specific capture of HDL by
 181 anti-ApoB. In both negative controls, the non-specific capture rate of < 15% is significantly lower than
 182 the specific capture rate of 80%. We benchmarked our method to a commercial immuno-capture kit using
 183 their standard protocol (see supporting information). As shown in Figure 3c, for nanobeads, only 20%
 184 HDL were captured by the μ Column (Milyteni Biotech) because of the low bead capture efficiency of
 185 the packed column. Furthermore, for microbeads like Dynabeads™, even after 16 hrs of incubation,
 186 which is much longer than the standard protocol, the HDL capture efficiency does not exceed 50%. For
 187 the same incubation time of 1 hr as the nanobeads, only 25% HDL was recovered (Figure S4), marginally
 188 > 15% non-specific capture rate.

189

190 To further demonstrate the advantage of the MNM immunocapturing method, miRNA extraction and
 191 qRT-PCR quantification of miR-21 were performed on HDL captured by both MNM and Dynabeads™.
 192 Figure 3d shows a Ct difference of more than 6 between the two immuno-capture methods, which sug-
 193 gests the miRNA expression result of Dynabeads™ is 64-fold lower than that of MNM (delta-delta Ct
 194 method). The long incubation time required by microbeads causes sample degradation and miRNA deg-
 195 radation, and adsorption, which leads to significant bias in miRNA quantification. In contrast, a high
 196 concentration of miR-21 was preserved in the fast MNM immunocapture.

197

198 2.4 Purification of EVs in Filtered Plasma

199 In this demonstration, 100 μ L healthy human plasma was first diluted and processed by tangential flow
 200 filtration with 30nm asymmetric nanoporous membranes³³ to remove most of the HDL and other

201 lipoproteins. As shown in Figure 4b, there was still 17% cholesterol left from mostly LDL and VLDL
202 after filtration. A small amount of HDL could also be present in the filtered sample due to the dominant
203 amount of the HDL in the original plasma. Therefore, we mixed the filtered sample with 2 μ g anti-ApoA-
204 I and 2 μ g anti-ApoB antibodies and incubated it for 30min. After adding 200 μ L anti-rabbit IgG mi-
205 croBeads (30nm, Milyteni Biotech) and incubating for 1 hr, the mixture was passed through the MNM.
206 The collected flow-through was the purified EV sample, which contained 85% of the original EV but
207 only 5% of the original cholesterol. The size distribution of the EV sample was also preserved after
208 purification, indicating minimal loss of EVs (Figures 4c and d).

209

210 **2.5 Isolation and Purification of EGFR EVs from DiFi Cell Lines**

211 A major research direction in the EV field is to identify EVs secreted from specific (diseased) cells or by
212 specific pathways¹⁴. In this study, EVs were first isolated from human colorectal cancer cells (DiFi) by
213 ANM (asymmetrical nanoporous membrane). Then specific EVs with EGFR membrane proteins were
214 isolated by the MNM to accurately quantify the miRNA content of specific EVs. Based on analysis of
215 EGFR-containing DiFi EVs, isolated EVs were likely exosomes based on tetraspanin content³⁴. Some
216 of the EVs released by the DiFi cells exhibited inactive EGFR and active EGFR³⁴. We utilized a total
217 EGFR antibody that captures both active and inactive EGFR in this experiment. DiFi cell culture super-
218 natants were first processed by tangential flow filtration with 30nm asymmetric nanoporous mem-
219 branes³³ to remove free-floating proteins. Briefly, 1 μ g anti-EGFR antibodies were added to the sample
220 and incubated for 30min. After adding 100 μ L anti-rabbit IgG microBeads (30nm, Milyteni Biotech) and
221 incubating for 1 hr, the mixture was passed through the MNM. We extracted miRNA from all fractions
222 during the process and performed qRT-PCR to assess miR-21 levels. Figure 5b shows miRNA content
223 inside the isolated EGFR EVs, and the flow-through material adds up equally to the total miR-21 levels
224 in the original sample with a 21% error, which is insignificant considering qRT-PCR can only differen-
225 tiate 2-fold changes. The total amount of EGFR in the ANM isolate, and MNM flow through is also
226 measured by ELISA. A drop of close to 90% was achieved, indicating most EGFRs were captured in the
227 MNM EGFR isolate (Figure 5b inset). To further explore the quantification potential of our system, we
228 did the same experiment on both undiluted and 8 \times diluted ANM-processed DiFi samples. As shown in

229 Figure 5c, the 8.3-fold change in miR-21 expression level matches the dilution factor, suggesting our
230 high efficiency is consistent among different initial sample concentrations, which is important for quan-
231 titative biomarker studies.

232

233 **3 Discussion**

234 Here, we demonstrated the utility and efficiency of electroplated MNM with unique heterogeneous su-
235 perparamagnetic junctions. This method can achieve high-efficiency capture of superparamagnetic nano-
236 beads. We achieved almost 100% nanobead recovery from the solution at up to 5mL/hr on a single de-
237 vice. The uncaptured EVs can go through the straight pores and be collected in the flow-through. We
238 proved our device's efficiency and specificity using HDL as a model, with >80% of HDL particles re-
239 covered and minimal non-specific retention at less than 15%. The high and consistent yield of our system
240 provides quantification potential for studies of EVs, lipoproteins, and other extracellular RNA carriers.
241 We further demonstrated the performance of MNM in exosome capture, purification of HDL-enriched
242 EV samples, and EGFR-positive EVs characterization. Our platform is also applicable for other molec-
243 ular or virus immunocapture applications where capture efficiency and throughput are essential.

244

245 **4 Methods**

246 **4.1 Numerical Simulations**

247 COMSOL was used to model and simulate different nanopore structures to estimate the magnetic flux
248 density and its gradient. A two-dimensional (2D) axial-symmetry geometry model was used with the
249 Magnetic Fields, No Currents interface in the AC/DC module. The software built-in NiFe B-H curve was
250 used. A static magnetic flux density of 0.5T was applied at the far boundary of the model. The simulation
251 was conducted with a physics-controlled meshing of extremely fine elements. More details have been
252 shown in the Supporting Information.

253

254 4.2 Microscopy Imaging

255 Surface SEM images were taken with Magellan 400. For EV-captured membranes, 2% EMS-quality
256 paraformaldehyde aqueous solution was used for fixation, and 2nm gold was sputtered in advance for
257 conductivity. Vesicles were examined under low beam energies. Cross-sections of the nanopores were
258 prepared using the Helios G4 UX DualBeam (Thermo Scientific). After protecting the cross-section sur-
259 face with Pt EBID, slices of 5nm thickness were sequentially obtained with Auto Slice & View™ 4
260 (AS&V4) software operating with a focused 10keV beam of gallium ions. The slicing was stopped at the
261 center of the pore, and the images were acquired with a voltage of 3kV using a TLD detector for second-
262 ary electrons.

263

264 4.3 Ni₈₀Fe₂₀ Deposition by Electroplating

265 The used track-etched PET films (PET115745, Wuwei Kejin Xinfu) are 11 μm thick and has a pore den-
266 sity of $5 \times 10^7/\text{cm}^2$. To fabricate the electroplated magnetic nanoporous membrane, 80nm Au was depos-
267 ited onto the track-etched PET films in an FC-1800 Evaporator. The gold layer provides good adhesive-
268 ness between polymer and NiFe and functions as a seed layer for electroplating. The membrane was cut
269 into 4cm × 4cm pieces. Copper tapes were used to fix membranes onto the support and electrically con-
270 nected to the cathode. A nickel plate was used as the anode. The electroplating solution adopted from the
271 literature^{35,36} can be found in Table S1. Constant current density at 2mA/cm² was applied by Keithley
272 2636A Dual-Channel System SourceMeter; voltage is monitored during the electroplating process. A
273 custom electroplating stirring tank was designed for uniform deposition. The deposition rate was derived
274 by SEM images on thicker samples grown under the same conditions. Another 10nm Au was deposited
275 on the top of the NiFe layer to reduce non-specific adsorption and chemical instability.

276

277 4.4 Ni₈₀Fe₂₀ Deposition by Sputtering

278 Same as the electroplated samples, 80nm Au were deposited onto the PET films initially. The sputtered
279 samples were prepared at room temperature in a commercial UHV sputtering system Oerlikon DCSS
280 using a Ni₈₀Fe₂₀ target. Ar gas flow was fixed to 20sccm, and the plasma power was 50W during depo-
281 sition. The deposition rate was derived by means of a stylus profilometer and SEM images on thicker

282 samples grown under the same conditions. After sputtering, 10nm Au was deposited at the top of the
283 NiFe layer.

284

285 **4.5 Plasma Samples**

286 De-identified plasma samples were obtained from Zen-Bio Inc. and consisted of 10mL of fresh human
287 plasma collected in tubes with EDTA coagulant. Each sample was tested for pathogens as required by
288 the FDA. All assay protocols performed in studies involving human participants were in accordance with
289 the ethical standards of University of Notre Dame.

290

291 **4.6 DiFi Cell Culture Conditioned Media Collection**

292 DiFi cells were grown in a C2011 FiberCell bioreactor with 20kDa pore using the manufacturer's in-
293 structions (FiberCell Systems, New Market, MD) using FiberCell systems' defined serum-free media
294 (CDM-HD). Specifically, the bioreactor was washed overnight with sterile 1X DPBS (Corning, Corning,
295 NY) and then overnight with high glucose DMEM (hgDMEM/ Corning). The bioreactor was treated
296 with 0.5mg of bovine fibronectin (Sigma, St. Louis, MO) in 20ml of DMEM for 4 hrs to overnight. The
297 bioreactor was then washed overnight with complete hgDMEM with 10% bovine growth serum (1%
298 Penicillin-Streptomycin [Pen/Strep, GIBCO, Dublin/Ireland], 1% Glutamine [GIBCO], 1% glutamine
299 [GIBCO], 1% non-essential amino acids [GIBCO]). The bioreactor was loaded with $1-5 \times 10^8$ DiFi cells
300 in complete hgDMEM with 10% serum and allowed to stand for 1 hr before circulating complete DMEM
301 with 10% serum. Glucose levels were monitored daily with a glucometer (CESCO bioengineering, Tre-
302 vose, PA), and when glucose levels were at half of that in starting media, the media bottle was replaced.
303 In subsequent media changes, the bioreactor went from 10% bovine serum to 5% then to 3%, before
304 switching to 10% CDM-HD (DMEM-HD) media. Once cells are established in DMEM-HD (at least two
305 weeks in DMEM-HD) routine harvest of conditioned media was performed, removing 20ml of condi-
306 tioned media per day. Collected media was spun at 2000 RPMs to remove cells and any large debris,
307 then a subfraction of the media was additionally gravity filtered through a Millex 0.22um pore syringe
308 filter (Millipore Sigma, Burlington, MA). At least 3 days of filtered media collections were pooled.

309

310 **4.7 Lipoprotein Collection**

311 Plasma was collected from consented human participants under active Vanderbilt IRB protocols and
312 guidance. Blood was drawn into EDTA-containing collection tubes and immediately centrifuged to sep-
313 arate plasma. HDL and LDL were isolated from human plasma by KBr density-gradient ultracentrifuga-
314 tion (DGUC), as previously described³². Briefly, native LDL (1.019-1.062g/L) and HDL (1.063-
315 1.021g/L) were isolated by sequential DGUC using an Optima XPN-80 Ultracentrifuge with SW41Ti or
316 SW32Ti rotors (Beckman-Coulter). HDL and LDL were dialyzed in PBS with >4 buffer changes and
317 concentrated with 3,000 Da m.w. cutoff filters (Millipore). Total protein levels were determined for each
318 lipoprotein sample (HDL and LDL) by BCA colorimetric assays (Pierce, ThermoFisher).

319

320 **4.8 Cholesterol Assay**

321 Cholesterol Quantification Assay Kit (Sigma-Aldrich, CS0005) was used to measure the cholesterol con-
322 centration of samples. Briefly, 44 μ L Assay Buffer, 2 μ L Probe, 2 μ L Enzyme Mix, 2 μ L Cholesterol Es-
323 terase, and 50 μ L sample were mixed and incubated at 37°C for 30min in each well. A calibration curve
324 was established for every measurement with standard samples with 0-5 μ g cholesterol. All samples were
325 diluted to the range of calibration curve with the Assay Buffer. Absorbance at 570nm was measured and
326 compared to the standards on the same plate to determine total cholesterol.

327

328 **4.9 qRT-PCR**

329 miRNAs were isolated from samples using the NucleoSpin® miRNA Plasma Kit (Takara Bio) according
330 to the manufacturer's manual. 300 μ L of the sample was first mixed with 90 μ L MLP solution and incu-
331 bated at room temperature for 3min, followed by adding 30 μ L MPP buffer and 1min room temperature
332 incubation. 3.5 μ L (1.6 \times 10⁸ copies/ μ L) of cel-miR-39-3p in RNase-free water was added into the lysate
333 as a normalization spiked-in control. Then the mixture was centrifuged at 11000 \times g. The supernatant was
334 taken and mixed with 400 μ L isopropanol. The mixture was transferred into the binding column and
335 centrifuged at 11000 \times g for 30s. The column was then washed with 100 μ L MW1 and 700 μ L MW2 se-
336 quentially at 11000 \times g for 30s, followed by 250 μ L MW2 washing and drying at 11000 \times g for 3min. Fi-
337 nally, 30 μ L RNase-free water was added to elute the miRNA at 11000 \times g for 1min after incubation at

338 room temperature for 1min. Reverse transcription was carried out using a miScript II RT Kit (Qiagen).
339 A 20 μ L reverse transcription reaction was prepared with 2.2 μ L of eluted miRNA, 4 μ L 5 \times miScript
340 HiSpec Buffer (Qiagen), 2 μ L 10 \times miScript Nucleic Mix (Qiagen), 9.8 μ L RNase-free water, and 2 μ L
341 miScript Reverse Transcriptase Mix (Qiagen). The reaction was incubated at 16 $^{\circ}$ C for 60 min, followed
342 by 95 $^{\circ}$ C for 5 min. The reverse transcription reaction was then diluted with 200 μ L RNase-free water.
343 Triplicates of qPCR reactions were carried out using miScript SYBR Green PCR Kit (Qiagen) and run
344 on a StepOnePlusTM Real-Time PCR System (Applied Biosystems). The reaction contained 2 μ L diluted
345 cDNA, 12.5 μ L 2 \cdot QuantiTect[®] SYBR Green PCR Master Mix (Qiagen), 2.5 μ L 10 \cdot miScript Universal
346 Primer (Qiagen), 10 \cdot miScript Primer Assay (Qiagen) for the target miRNA, and 5.5 μ L RNase-free water
347 in a final volume of 25 μ L. The reaction mixtures were incubated for 15 min at 95 $^{\circ}$ C, followed by 45
348 cycles of 94 $^{\circ}$ C for 15 s, 55 $^{\circ}$ C for 30 s, and 70 $^{\circ}$ C for 30 s. The C_q values were acquired and analyzed
349 using StepOneTM Software v2.3 in accordance with the MIQE guidelines (Bustin et al., 2013). The C_q
350 values of the target miRNAs were adjusted by spiked-in standard control (cel-miR-39-3p) added during
351 miRNA extraction.

352

353 **4.10 ELISA**

354 A human EGFR ELISA kit (EGFR0, R&D SystemsTM) was used to quantify the EGFR in the samples.
355 100 μ L of Assay Diluent and 50 μ L of standard, control, or sample were added to each well in the mi-
356 croplate, followed by 2 hrs incubation at room temperature. After 4 times of aspirating and washing each
357 well, 200 μ L of Human EGFR Conjugate was added to each well and incubated for 2 hrs at room tem-
358 perature, followed by 4 washes. 200 μ L of Substrate Solution was added to each well and incubated for
359 30 minutes at room temperature, and then 50 μ L of Stop Solution was added to each well. Absorbance
360 at 450nm subtracted by readings at 540nm was measured. The EGFR concentration was determined by
361 the readings and the established calibration curve.

362

363 **4.11 Nanoparticle Tracking Analysis**

364 Nanoparticle tracking analysis (NTA) was performed using a NanoSight NS300 (NanoSight Ltd., Ames-
365 bury, UK). All samples were diluted to the optimal working particle range prior to measurements using

366 1×PBS. Five 60s videos were recorded of each sample with the camera level set at 10. A constant flow
367 rate setting of 1000 was maintained during the recording. The temperature was monitored throughout the
368 measurements. The instrument was flushed with 1×PBS between measurements. Videos recorded for
369 each sample were analyzed with NTA software to determine the concentration and size distribution of
370 measured particles with corresponding standard error. The same detection threshold was used for analy-
371 sis.

372 **5 Conflicts of interest**

373 There are no conflicts to declare.
374

375 **6 Data availability**

376 The data that support the findings of this study are available within the article and Supplementary Infor-
377 mation files or available from the corresponding authors on request. Source data are provided in this
378 paper.

379 **7 Acknowledgments**

380 The authors acknowledge the support of the NIH Common Fund through the Office of Strategic Coordi-
381 nation/Office of the NIH Director, 1UH3CA241684-01. C.Z. acknowledge the support of a China Schol-
382 arship Council fellowship. R.J.C. acknowledges the support of NCI R35 CA197570. The authors
383 acknowledge the support of the Cancer Cure Venture (CCV) Grant, made possible by the Walther Cancer
384 Foundation.

385

386 **8 Author Contributions**

387 C.Z. and X.H. contributed equally to this work. C.Z., X.H., C.W., and H.C.C. conceived the idea and
388 designed the study. C.Z. performed the finite element simulations. C.Z., X.H., and C.W. performed the
389 experiments. C.Z. analyzed the results and wrote the manuscript with inputs from all authors. Y.Z., L.X.,

390 J.N.H., J.L.F, K.C.V., and R.J.C. provided biological samples. C.W., S.S., and H.C.C. supervised the
391 project.

392

393 **References**

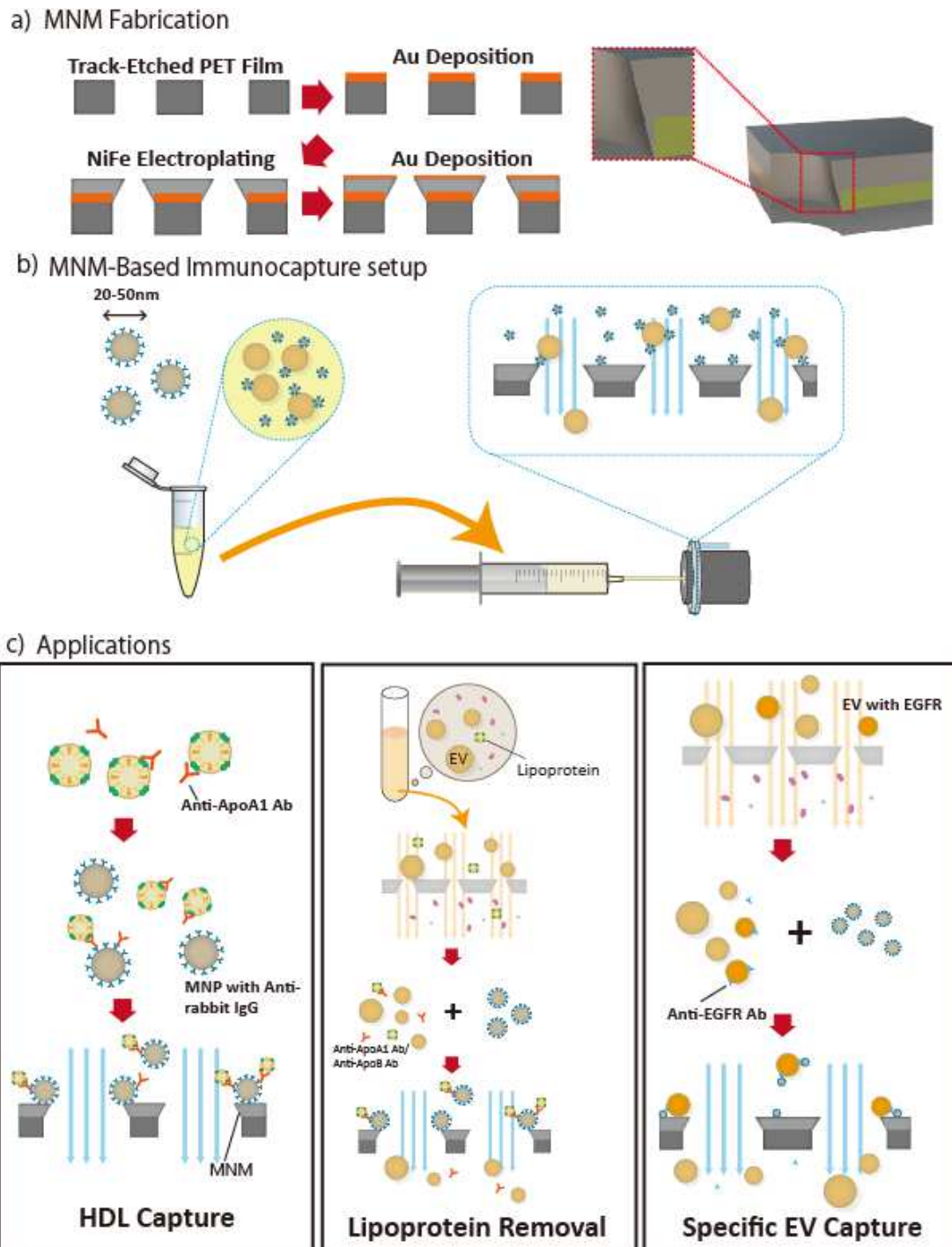
- 394 1. Valadi, H. *et al.* Exosome-mediated transfer of mRNAs and microRNAs is a novel mechanism of
395 genetic exchange between cells. *Nat. Cell Biol.* **9**, 654–659 (2007).
- 396 2. Mathivanan, S., Ji, H. & Simpson, R. J. Exosomes: extracellular organelles important in intercellular
397 communication. *J. Proteomics* **73**, 1907–1920 (2010).
- 398 3. Simonsen, J. B. What Are We Looking At? Extracellular Vesicles, Lipoproteins, or Both? *Circ. Res.*
399 **121**, 920–922 (2017).
- 400 4. Vlassov, A. V., Magdaleno, S., Setterquist, R. & Conrad, R. Exosomes: current knowledge of their
401 composition, biological functions, and diagnostic and therapeutic potentials. *Biochim. Biophys. Acta*
402 **1820**, 940–948 (2012).
- 403 5. Jeppesen, D. K. *et al.* Reassessment of Exosome Composition. *Cell* **177**, 428–445.e18 (2019).
- 404 6. Zhuang, G. *et al.* Tumour-secreted miR-9 promotes endothelial cell migration and angiogenesis by
405 activating the JAK-STAT pathway. *EMBO J.* **31**, 3513–3523 (2012).
- 406 7. Hunter, M. P. *et al.* Detection of microRNA Expression in Human Peripheral Blood Microvesicles.
407 *PLoS ONE* **3**, (2008).
- 408 8. Minciacchi, V. R., Freeman, M. R. & Di Vizio, D. Extracellular Vesicles in Cancer: Exosomes,
409 Microvesicles and the Emerging Role of Large Oncosomes. *Semin. Cell Dev. Biol.* **40**, 41–51
410 (2015).
- 411 9. Fujita, Y., Yoshioka, Y. & Ochiya, T. Extracellular vesicle transfer of cancer pathogenic compo-
412 nents. *Cancer Sci.* **107**, 385–390 (2016).
- 413 10. Kosaka, N., Yoshioka, Y., Fujita, Y. & Ochiya, T. Versatile roles of extracellular vesicles in cancer.
414 *J. Clin. Invest.* **126**, 1163–1172 (2016).
- 415 11. Cromwell, W. C. & Otvos, J. D. Heterogeneity of low-density lipoprotein particle number in patients
416 with type 2 diabetes mellitus and low-density lipoprotein cholesterol <100 mg/dl. *Am. J. Cardiol.*
417 **98**, 1599–1602 (2006).

- 418 12. Crescitelli, R. *et al.* Distinct RNA profiles in subpopulations of extracellular vesicles: apoptotic
419 bodies, microvesicles and exosomes. *J. Extracell. Vesicles* **2**, 20677 (2013).
- 420 13. Akinkuolie, A. O., Paynter, N. P., Padmanabhan, L. & Mora, S. High-density lipoprotein particle
421 subclass heterogeneity and incident coronary heart disease. *Circ. Cardiovasc. Qual. Outcomes* **7**,
422 55–63 (2014).
- 423 14. Coumans, F. A. W. *et al.* Methodological Guidelines to Study Extracellular Vesicles. *Circ. Res.* **120**,
424 1632–1648 (2017).
- 425 15. Willms, E., Cabañas, C., Mäger, I., Wood, M. J. A. & Vader, P. Extracellular Vesicle Heterogeneity:
426 Subpopulations, Isolation Techniques, and Diverse Functions in Cancer Progression. *Front. Immu-*
427 *nol.* **9**, (2018).
- 428 16. Wu, Y., Deng, W. & Klinke, D. J. Exosomes: Improved methods to characterize their morphology,
429 RNA content, and surface protein biomarkers. *The Analyst* **140**, 6631–6642 (2015).
- 430 17. Jeyaram, A. & Jay, S. M. Preservation and Storage Stability of Extracellular Vesicles for Therapeu-
431 tic Applications. *AAPS J.* **20**, 1 (2017).
- 432 18. Clayton, A. *et al.* Analysis of antigen presenting cell derived exosomes, based on immuno-magnetic
433 isolation and flow cytometry. *J. Immunol. Methods* **247**, 163–174 (2001).
- 434 19. Mathivanan, S. *et al.* Proteomics analysis of A33 immunoaffinity-purified exosomes released from
435 the human colon tumor cell line LIM1215 reveals a tissue-specific protein signature. *Mol. Cell.*
436 *Proteomics MCP* **9**, 197–208 (2010).
- 437 20. Koga, K. *et al.* Purification, characterization and biological significance of tumor-derived exosomes.
438 *Anticancer Res.* **25**, 3703–3707 (2005).
- 439 21. Issadore, D., YELLESWARAPU, V. & KO, J. Magnetic separation filters and microfluidic devices
440 using magnetic separation filters. (2017).
- 441 22. Ko, J. *et al.* Combining Machine Learning and Nanofluidic Technology To Diagnose Pancreatic
442 Cancer Using Exosomes. *ACS Nano* **11**, 11182–11193 (2017).
- 443 23. Thamida, S. K. & Chang, H.-C. Nonlinear electrokinetic ejection and entrainment due to polariza-
444 tion at nearly insulated wedges. *Phys. Fluids* **14**, 4315–4328 (2002).
- 445 24. Wang, C., Sensale, S., Pan, Z., Senapati, S. & Chang, H.-C. Slowing down DNA translocation
446 through solid-state nanopores by edge-field leakage. *Nat. Commun.* **12**, 140 (2021).

- 447 25. Barbry, M. *et al.* Atomistic Near-Field Nanoplasmonics: Reaching Atomic-Scale Resolution in Na-
448 noplasmonics. *Nano Lett.* **15**, 3410–3419 (2015).
- 449 26. Imura, K., Nagahara, T. & Okamoto, H. Near-Field Two-Photon-Induced Photoluminescence from
450 Single Gold Nanorods and Imaging of Plasmon Modes. *J. Phys. Chem. B* **109**, 13214–13220 (2005).
- 451 27. Wang, Y., Plouraboue, F. & Chang, H.-C. Broadband converging plasmon resonance at a conical
452 nanotip. *Opt. Express* **21**, 6609–6617 (2013).
- 453 28. El-makadema, A., Rashid, L. & Brown, A. K. Geometry Design Optimization of Large-Scale Broad-
454 band Antenna Array Systems. *IEEE Trans. Antennas Propag.* **62**, 1673–1680 (2014).
- 455 29. Eteng, A. A., Abdul Rahim, S. K. & Leow, C. Y. Geometrical Enhancement of Planar Loop Anten-
456 nas for Inductive Near-Field Data Links. *IEEE Antennas Wirel. Propag. Lett.* **14**, 1762–1765 (2015).
- 457 30. Wang, Y., Chang, T. C. & Stoddart, P. R. Diffraction-limited ultrasensitive molecular nano-arrays
458 with singular nano-cone scattering. *Biomicrofluidics* **8**, 10–14 (2014).
- 459 31. Pegg, L.-J. & Hatton, R. A. Nanoscale Geometric Electric Field Enhancement in Organic Photovol-
460 taics. *ACS Nano* **6**, 4722–4730 (2012).
- 461 32. Michell, D. L. *et al.* Isolation of High-density Lipoproteins for Non-coding Small RNA Quantifica-
462 tion. *J. Vis. Exp. JoVE* (2016) doi:10.3791/54488.
- 463 33. Wang, C., Senapati, S. & Chang, H.-C. Liquid biopsy technologies based on membrane microfluid-
464 ics: High-yield purification and selective quantification of biomarkers in nanocarriers.
465 *ELECTROPHORESIS* **41**, 1878–1892 (2020).
- 466 34. Zhang, Q. *et al.* Supermeres are functional extracellular nanoparticles replete with disease bi-
467 omarkers and therapeutic targets. *Nat. Cell Biol.* **23**, 1240–1254 (2021).
- 468 35. Smistrup, K., Tang, P. T. & Moller, P. Pulse Reversal PermAlloy Plating Process for MEMS Ap-
469 plications. *ECS Trans.* **3**, 179–189 (2007).
- 470 36. Schiavone, G. *et al.* Integration of Electrodeposited Ni-Fe in MEMS with Low-Temperature Depo-
471 sition and Etch Processes. *Materials* **10**, (2017).

472

473



474

475

476

477

478

479

480

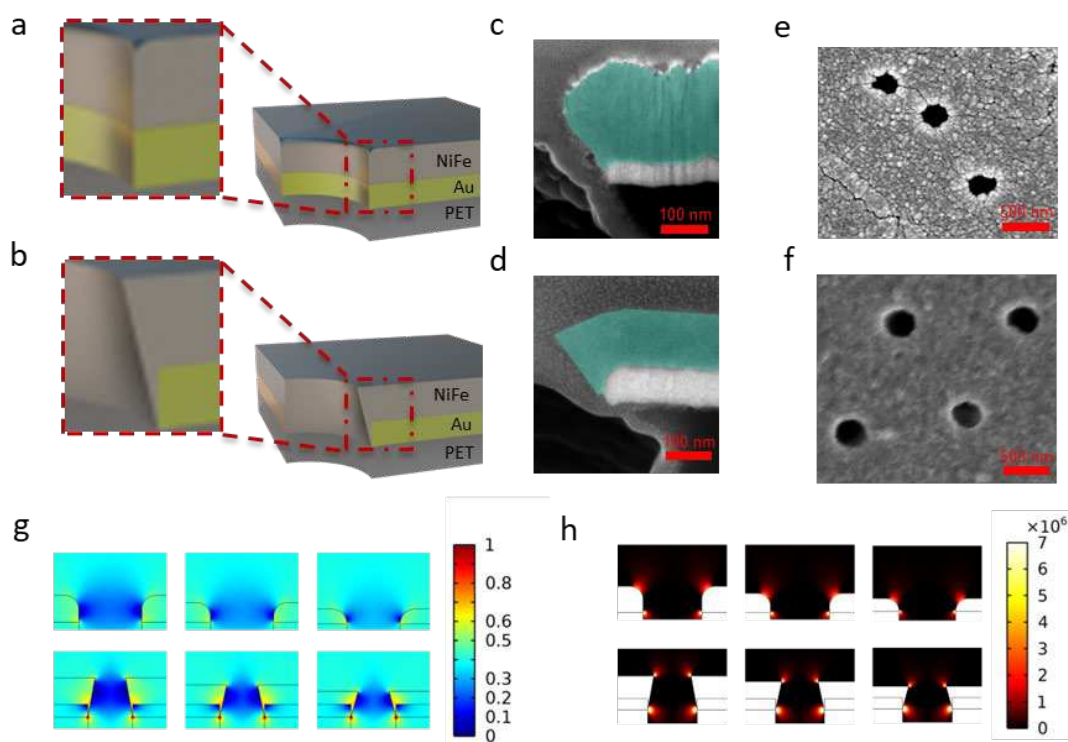
481

482

483

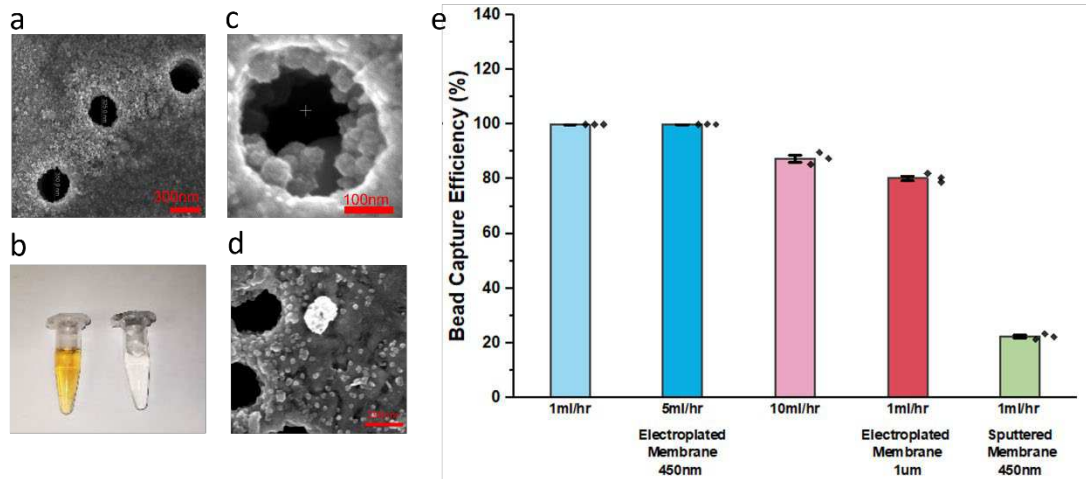
Schematic 1. Schematic of the experimental procedure. a) Fabrication of the magnetic nanoporous membrane (MNM). 80nm Au was deposited onto the tracked-etched PET film to provide good adhesion and electric conductivity for electroplating. Then 200nm NiFe film was deposited onto the membrane with electroplating. 10nm Au was deposited finally to reduce non-specific adsorption and chemical instability. (On the right) The heterogeneous nano edge junction at the edge of the nanopore on the membrane is highlighted. b) MNM-based immunocapture setup. First, the antibody and antigen were incubated to form an Ab-Ag complex, followed by incubating with magnetic nanobeads, which were conjugated with anti-rabbit IgG antibodies. Then the diluted sample was run through the chamber of the MNM device with a syringe and pump. The MNM device was assembled with the MNM sandwiched between

484 two 3D-printed chips. The device was assembled between two magnets, with the magnet near the inlet
 485 in a ring shape. The magnetic beads were captured onto the edge of the nanopores, as highlighted. c)
 486 Experimental steps of the three applications. Anti-ApoA1 antibodies were used to capture HDL; an
 487 Asymmetric nanopore membrane was used to isolate the EVs, with a small amount of HDL remaining,
 488 and we used MNM to remove the residual HDL to purify the EV fraction; In the EV fraction, MNM was
 489 utilized to capture the specific EV with particular surface protein, i.e., EGFR.
 490



491
 492 **Figure 1.** Characterization of the nanopores on the sputtered and electroplated MNM. Schematic of
 493 the nanopores on a) a sputtered magnetic nanoporous membrane, and b) an electroplated magnetic na-
 494 nanoporous membrane, and the edge of the nanopore is highlighted. (The final thin gold layer is ignored)
 495 c) Cross-section SEM images of a single nanopore on a sputtered magnetic nanoporous membrane. Note
 496 the smooth edge of the NiFe layer (blue). d) Cross-section SEM images of a single nanopore on an
 497 electroplated magnetic nanoporous membrane. Note the sharp edge of the NiFe layer (blue). SEM images
 498 of the e) electroplated membrane and f) sputtered membrane. g) Simulation of magnetic flux density (T)
 499 in nanopores on ideal sputtered magnetic nanoporous membrane (upper) and ideal electroplated magnetic
 500 nanoporous membranes (lower), showing the dramatic amplification of the flux density at the wedge on
 501 the electroplated MNM (Membrane thickness left to right: 200nm, 150nm, 100nm). h) Simulation of the
 502 magnetic field, showing the gradient of flux density norm square (T^2/cm) at the wedge on both ideal
 503 sputtered magnetic nanoporous membranes (upper) and ideal electroplated magnetic nanoporous mem-
 504 branes (lower) (Membrane thickness left to right: 200nm, 150nm, 100nm).

505
 506



507

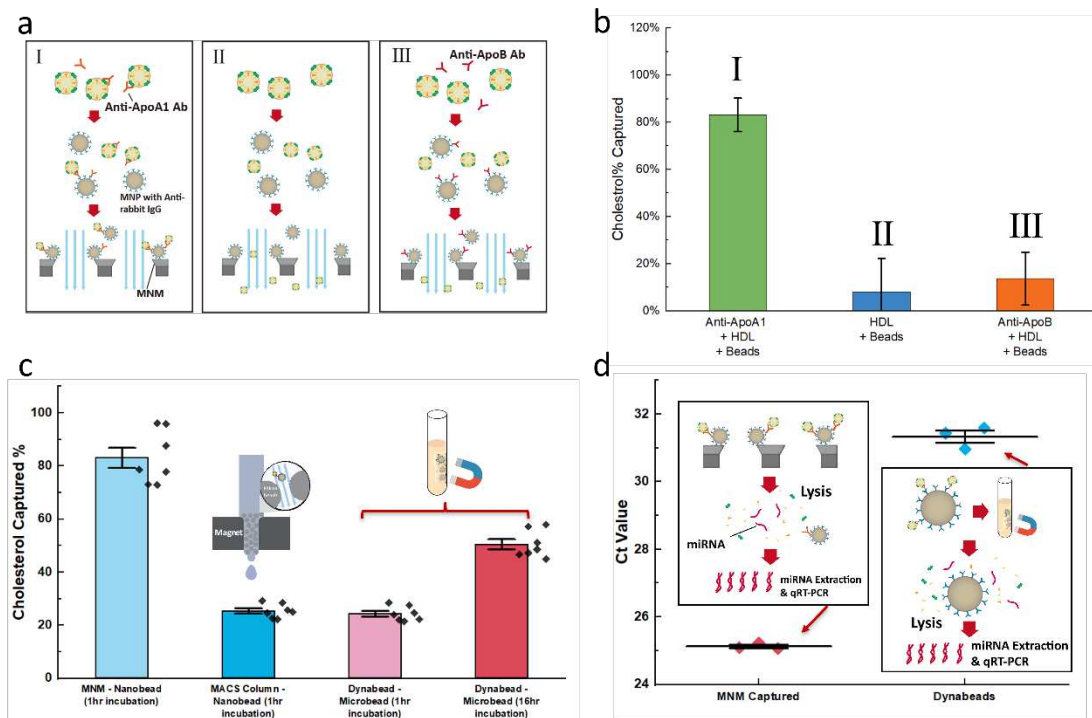
508

Figure 2. Characterization of the magnetic beads capture of MNM. a) SEM image of captured mag-
 509 netic beads near the edges of nanopores by the monopole field. The diameter of the pore has decreased
 510 to around 300nm after the deposition of different metallic layers. b) Solution of beads before passing
 511 through the magnetic nanoporous membrane (left) and after filtering through the magnetized membrane
 512 (right). The yellow color indicates the concentrated beads. c) Zoomed-in SEM image shows nanobeads
 513 captured inside a single nanopore by the dipole field of the wedge junction. d) SEM image of mouse
 514 plasma exosome captured near the nanopore. e) Bead capture efficiency of sputtered and electroplated
 515 membranes at different flow rates and pore sizes. For the electroplated membrane, the original pore size
 516 of 450nm and 1µm and flow rate of 1mL/hr, 5mL/hr, and 10mL/mL have been tested. For the sputtered
 517 membrane, the original pore size of 450nm and flow rate of 1mL/hr have been tested.

518

519

520

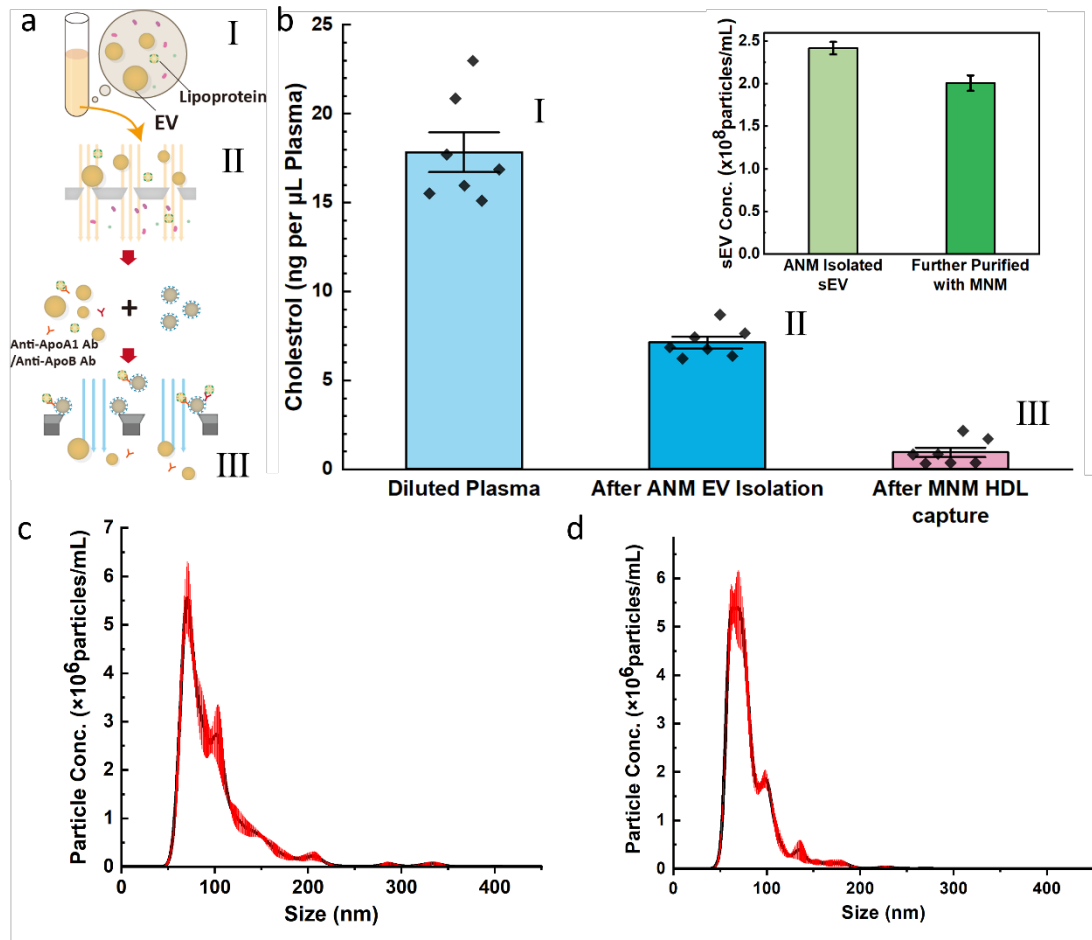


521

522 **Figure 3.** Characterization of the HDL capture rate using cholesterol as a measure. a) Schematic of the immunocapture of HDL cap-
 523 ture rate using cholesterol as a measure. In the three cases, different combinations were tested for specific
 524 capture of HDL with anti-ApoA1 antibodies and non-specific capture with no antibodies and anti-ApoB
 525 antibodies, which are specific to LDL. b) Capture rate of the three cases in a). c) Comparison of HDL
 526 capture rate using different immunocapture kits, including the Miltenyi MACS™ μ Column and Ther-
 527 mofisher Dynabeads™. The inset schematics show the basic working principle of different technologies.
 528 The incubation time was chosen to be 1h and 16h for Dynabeads™. d) Ct value of miR-21 from qRT-
 529 PCR experiments. MiRNA samples were extracted from HDL captured by both MNM and Dynabeads™
 530 with the same starting sample volume. The incubation time of the MNM experiment is 1h, and that of
 531 Dynabeads™ is 12h. The schematics of the immunocapture and qRT-PCR were shown in the inset. The
 532 HDL was captured by MNM or Dynabeads and then lysed, followed by miRNA extraction and qRT-
 533 PCR.

534

535

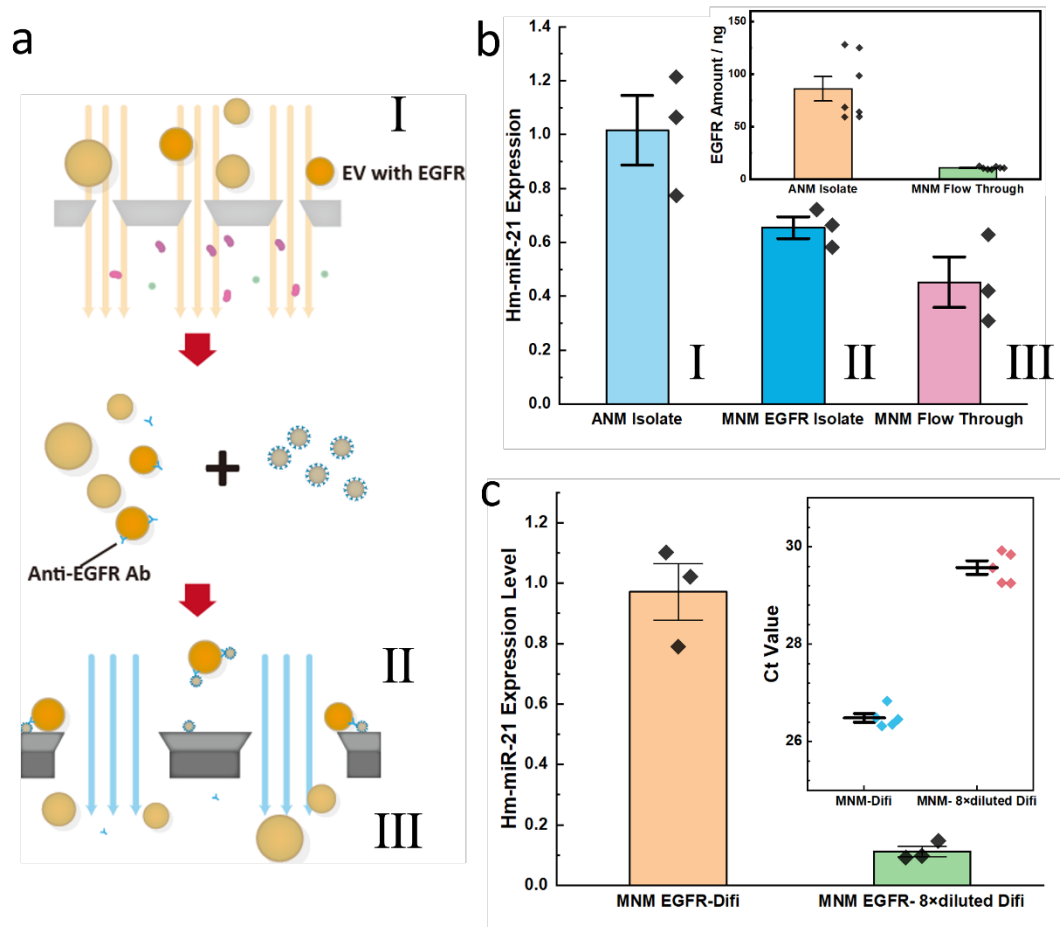


536

537

Figure 4. Characterization of the HDL removal from the fractionated EV. a) Schematic of the EV fractionation and immunocapture of HDL. The diluted plasma (sample I) runs through the asymmetric nanoporous membrane to remove other particles with a size-exclusion mechanism, thus obtaining the EV fraction (sample II). Due to the dominating amount of HDL, a small portion of HDL remained in the EV fraction, so it was incubated with anti-ApoA1 and anti-ApoB antibodies, and then magnetic nano-beads conjugated with anti-rabbit IgG antibodies and run through the MNM device to remove the HDL, and the flow-through was collected (sample III). b) Lipoproteins (cholesterol) remnant at different stages of purification from samples I, II, III in a), and (inset) EV concentration before and after MNM immunocapture (sample II and III). Size distribution of EV samples with NTA c) before (sample II) and d) after MNM immunocapture (sample III).

547



548

549

550

551

552

553

554

555

556

557

558

559

Figure 5. Characterization of the immunocapture of specific EV, i.e., EV with EGFR. a) Schematic of the EV fractionation and immunocapture of EV with EGFR. The DiFi cell culture medium was run through the asymmetric nanoporous membrane to obtain the EV fraction (sample I), which was then incubated with the anti-EGFR antibodies and then magnetic nanobeads conjugated with anti-human IgG antibodies. Then the samples passed through the MNM device, with the captured sample on the magnetic membrane mixed with lysing buffer (sample II), and the flow-through was collected (sample III). b) Hm-miR-21 expression level of different DiFi exosome fractions from samples I, II, III in a). The total amount of EGFR was also measured for I and III. c) Expression level of Hm-miR-21 in the EGFR exosomes before and after 8× dilution of the DiFi samples and the Ct value of their qRT-PCR results.

Supplementary Files

This is a list of supplementary files associated with this preprint. Click to download.

- [CommBioSubmissionSI.pdf](#)